Understanding process-microstructure-property relationships in laser powder bed fusion of non-spherical Ti-6Al-4V powder

Mohammadreza Asherloo ^a, Junghyun Hwang ^{a,1}, Ryan Leroux ^{b,2}, Ziheng Wu ^{c, 3}, Kamel Fezzaa ^d, Muktesh Paliwal ^e, Anthony D. Rollett ^c, Amir Mostafaei ^{a, *}

- ^a Department of Mechanical, Materials and Aerospace Engineering, Illinois Institute of Technology, 10 W 32nd Street, Chicago, IL 60616, USA
- ^b Department of Materials Science and Engineering, University of California, Los Angeles, CA, USA.
- ^c Department of Materials Science and Engineering, Carnegie Mellon University, Pittsburgh, PA, 15213, USA
- ^d The Advanced Photon Source, Argonne National Laboratory, Lemont, IL, United States of America
- ^e Kymera International Reading Alloys, Robesonia, PA 19551, USA

Abstract

Powder feedstock is a major cost driver in metal additive manufacturing (AM). Replacing the spherical powder with the cost-efficient non-spherical one can reduce the feedstock cost up to 50% and attract more interest to adopt AM in production and new alloy development. Here, a comprehensive study was conducted to understand process-microstructure-property relationships in laser powder bed fusion of hydride-dehydride Ti-6Al-4V powder. We demonstrated that variation of laser scan speed had a significant impact on the grain structure, pore evolution and properties compared to laser power. Dynamic X-ray radiography showed that with decreasing scan speed at a constant laser power, a transition from conduction to keyhole mode laser processing occurred, in which a deeper melt pool at lower scan speed intensified texture. In other words, an increase in laser scan speed resulted in formation of the refined prior β grains with shape factor of ~5, lowering the anisotropy. The degree of variant selection was evaluated based on the analyzed texture as a function of laser power and scan speed. With increasing laser scan speed, the dominant α/α boundary type was altered from type 2 to 4 and the degree of variant selection was noticeably decreased. On the other hand, increasing laser power left the morphology of prior β grains, their size, and the dominant α/α boundary (type 4) unchanged, while the texture and anisotropy were intensified, and the degree of variant selection was slightly decreased. Finally, dependency of surface roughness and microhardness were discussed as a function of laser processing parameters.

Keywords: Additive manufacturing; Texture analysis; Synchrotron X-ray high-speed imaging; variant selection; Hardness.

¹ Now at: LG Energy Solution

² REU summer student awarded by National Science Foundation

³ Current affiliation: Materials Engineering Division, Lawrence Livermore National Laboratory, 7000 East Ave, Livermore, CA 94550, USA

^{*} Corresponding authors: A. Mostafaei (mostafaei@iit.edu)

1. Introduction

Among titanium alloys, Ti-6Al-4V is a popular material due to its desirable characteristics such as high strength, good fracture toughness, high corrosion resistance, great biocompatibility, and high strength-to-weight ratio [1]. These characteristics make this alloy suitable for various industries such as aerospace, automotive, and biomedical applications [2–4]. There are challenges with manufacturing of titanium alloy due to poor thermal conductivity, high strain hardening, and high affinity to react with oxygen at elevated temperatures [5–8]. Fusion-based additive manufacturing (AM) methods has attracted attentions due to design freedom, low material waste, and shortened product development [9], thus, AM processing of Ti-6Al-4V alloy could minimize challenges compared to the conventional manufacturing methods.

Various fusion-based AM methods have been adopted to process Ti-6Al-4V feedstock. Spherical powders produced by atomization are typical feedstock in powder-based AM due to acceptable powder flow and possible packing density of 55-60%, however, the cost of powder production and trapped gas within particles are major drawbacks of using this powder. Powder production via mechanical milling can be an alternative solution for titanium alloys. Non-spherical morphology was reported for Ti-6Al-4V powder produced by hydride-dehydride process (HDH) followed by mechanical milling [10–12]. The major challenges in using this new feedstock in powder bed AM is low flowability and packing density.

The replacement of gas atomized powder with HDH powder in AM presents significant challenges and necessitates thorough research into the underlying physics of laser-powder interaction, melt pool dynamics, and potential defect formation mechanisms, due to the non-spherical morphology of HDH powder [13]. Recent studies have investigated the use of non-spherical titanium powder in various powder bed AM processes, such as laser beam powder bed fusion (LB-PBF) and electron beam powder bed fusion (EB-PBF), with varying degrees of success. In a study by Medina [14], the potential cost savings of blending HDH titanium powder with spherical powder to reduce part production expenses were explored. The study found that using a double melting process in electron beam AM increased part density. By adopting a processing parameters optimization approach, Narra et al. [15] examined the feasibility of using HDH Ti-6Al-4V powder in the EB-PBF process, and found that a relative density greater than 99% can be achieved. In other reports [16,17], a mixture of spherical and non-spherical powders was LB-PBF processed and parts with relative densities of ~99% were achieved.

In our earlier studies, we examined the general printability of the non-spherical HDH powder using dynamic x-ray radiography (DXR) and identified a new defect formation mechanism resulting from its morphology compared to the spherical powder. Wu et al. [18] achieved up to 99.8% relative density in L-PBF processed non-spherical HDH Ti-6Al-4V powder but noted the potential for powder spreading resulting in patches of low packing density and non-continuous melt pool tracks. Specifically, a low-density site in the powder layer can create a cavity on the melted surface, causing the next layer of powder to have a locally thicker layer in the cavity that may not fully melt, leading to the formation of a lack-of-fusion pore. Asherloo et al. [19] optimized the process parameters to achieve a relative density of >99.8% by utilizing the process window approach. The flowability was tested based on the bulk flow energy (BFE) and the specific energy (SE) and it was reported that the non-spherical HDH powder with size distribution of 50-120 μm showed similar or even better behavior (BFE=341 mJ and SE=2.7 mJ/g) to that of the spherical powder with size distribution of 20-63 μm (BFE=365 mJ and SE=2.32 mJ/g) [19]. This could be related to better flowability of coarse non-spherical HDH powder compared to fine spherical

powders. Additionally, they demonstrated that the fatigue performance of the manufactured parts using non-spherical powder was comparable to those made with spherical powder. However, the control over the microstructure when using this HDH non-spherical powder has yet to be studied.

In laser powder bed fusion (L-PBF), each discrete layer of powder is selectively melted by laser followed by rapid cooling rates of the melt pool. The resultant grain structure of the as-built part relies on the AM processing and thermal history. A typical microstructure of an L-PBF processed Ti-6Al-4V shows columnar prior β grains [20], in which α' martensite phase is present in the prior β grains [21,22] as well as a small fraction (up to ~4%) of nanoscale β phase [23] and some orthorhombic α'' phase in the V super-enriched areas [24,25]. There are two practical ways to control microstructure including (1) in situ processing such as controlling the energy density and scanning strategy to create lamellar $\alpha+\beta$ structure in the as-built condition [26] and (2) ex situ methods such as various post-print heat treatments to alter microstructure in the as-built parts.

Microstructure control has been carried out by varying laser processing parameters during L-PBF process of Ti-6Al-4V powders. It has been reported [27] that at a constant volumetric energy density of 50.62 J/mm³, various microstructures can be attained. For example, decreasing the layer thickness and increasing the laser scan speed can result in presence of minor lamellar $\alpha+\beta$ in the dominant α' martensite phase. Moreover, decreasing the focal offset distance of the laser (i.e., increasing the laser spot size [28]) can change microstructure from α' martensite with minor lamellar $\alpha+\beta$ to lamellar $\alpha+\beta$ with minor α' martensite, known as *in situ* decomposition of α' . Yang *et al.* [21] showed that with increasing the laser scan speed up to 900 mm/s, the aspect ratio of α' martensite laths increased from ~22 to ~26, while further increase of the laser scan speed from 900 mm/s to 1100 mm/s reduced the aspect ratio to ~21.

Attempts have been made to study the texture evolution in the AM fabricated titanium alloys through variant selection analysis. Simonelli et al. [29] reported that the α' texture was random owing to the high fraction of small α' grains with random orientations. Moreover, the high cooling rate in the L-PBF process lowered prior β/β grain boundary α' growth. In electron beam PBF, Stephenson *et al.* [30] demonstrated that the variant selection can be impacted by scanning strategy. A raster scan strategy dominated self-accommodation, while random scan strategy led to the prior β grain boundary variant selection mechanism. A recent research by Asherloo *et al.* [31] revealed potential dependency of variant selection on powder morphology. Despite high cooling rates in L-PBF, it was shown that the α/α' originated from the β/β grain boundary, which could be attributed to the locally lowered cooling rates because of shadowing effect and less laser penetration.

Here, we aim to study the effects of altering two processing parameters, laser power (P) and scan speed (V), on porosity, surface roughness, microstructure, texture evolution, and microhardness. Advanced characterization tools such as synchrotron-based X-ray and electron backscatter diffraction are used to observe laser-powder interaction and texture, respectively. The presented quantitative and qualitative analyses help us to better understand the role of processing variables on the evolution of grain structure and variant selection during the solid-state phase transformation of $\beta \rightarrow \alpha$ in titanium-based alloys.

2. Experimental procedures

2.1. Ti-6Al-4V feedstock analysis

Non-spherical powder was provided by Kymera International – Reading Alloys. The nominal powder size distribution (PSD) of the powder was reported to be 50-120 μ m with the nominal composition given in [19]. The powder particles were dispersed directly on a carbon tape and placed on an FEI Aspex Express scanning electron microscope (SEM) holder. Then, imaging was conducted to collect micrographs from ~1,100 individual particles. The ImageJ software [32] was used to process the collected images. Results showed a bimodal PSD of 20-130 μ m, with d₁₀, d₅₀, and d₉₀ of 28 μ m, 82 μ m, and 103 μ m, respectively. Also, the mean particle size (d_{mean}) was 76 μ m and the average circularity was 0.68. Additionally, the morphology of the powder particles was confirmed by using a JEOL 5900LV SEM (see Figure 1a).

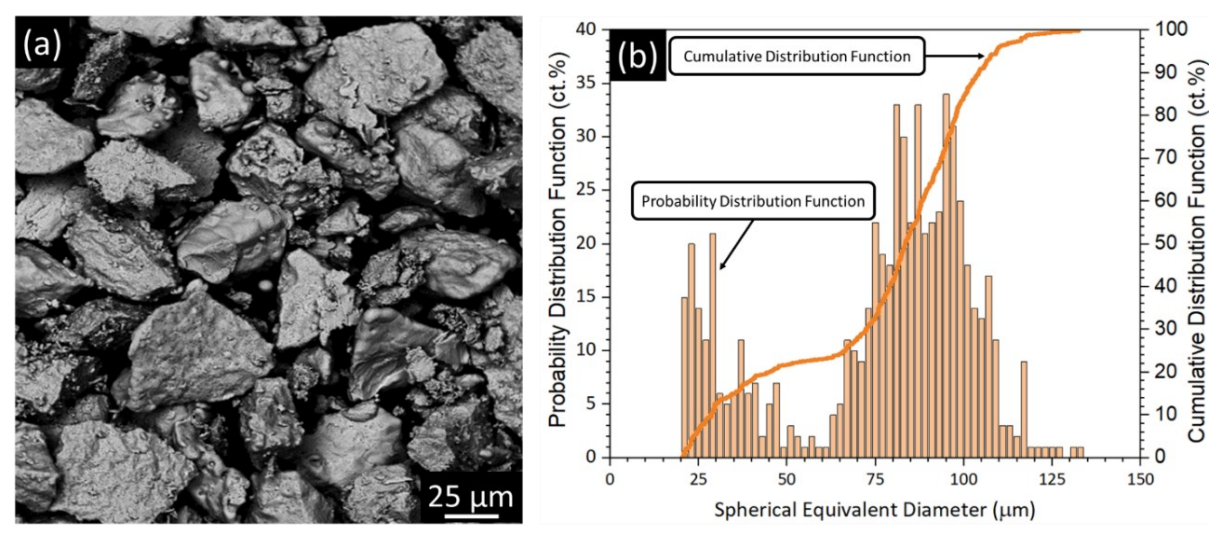


Figure 1. (a) Morphology observation using SEM and (b) PSD results of the used powder.

2.2. Laser powder bed fusion process

Coupons with dimensions of $15 \times 10 \times 10$ mm were manufactured using an EOS 290M L-PBF machine. Two sets of coupons were fabricated including (1) P = 370 W and varied V ranging 400-1500 mm/s and (2) V = 1250 mm/s and varied P ranging 225-370 W. The hatch spacing (H), layer thickness (L), and scan rotation were kept constant in all experiments at 120 μ m, 60 μ m, and 67°, respectively. The coupons were fabricated directly on the base plate. Powders were dispensed on the surface using a brush recoater blade. Note that the nominal sample properties were reported by the EOS company and the same data were used in the current study for comparison purposes.

2.3. Characterizations

Parts were removed from the base plate using an electrical discharge machining (EDM). After slicing samples parallel to the built direction, parts were hot-mounted (details can be found in [19]) followed by standard metallographic steps. Relative density of the parts was measure using optical micrographs from the cross-sections. Optical images were collected using a Nikon Eclipse MA200 optical microscope and analyzed using the ImageJ software [32]. Electron backscatter diffraction (EBSD) data was collected using an SEM (JEOL 5900LV) equipped with an EBSD detector (Oxford Instruments). Image collection and post-processing steps were done using AzTex and HKL Channel 5 software, respectively. Vickers microhardness measurements were conducted using a Buehler Micromet 2 machine under a load of 500 g and dwell time of 15 s and the average hardness of ten indentations was reported.

2.4. Dynamic X-ray Radiography (DXR)

The DXR experiments were performed at Argonne National Lab (32-ID-B beamline). A miniature single-bead powder bed setup was used as follows: a thin slab made of Ti-6Al-4V alloy (1 mm thick and 2.89 mm height) sandwiched between two 1 mm thick and 3 mm high glassy carbon plates, powder layer thickness of ~200 μ m, under Ar atmosphere with (1 atm). A laser (λ = 1040 nm, P_{max} = 540 W, spot diameter (Gaussian) = 71.5 μ m) was used to scan each melt track from the top. A 200- μ m powder layer was manually spread on top of a short thin slab (1 mm thickness × 2.89 mm height) of Ti-6Al-4 V sandwiched between two glassy carbon plates (1 mm thickness × 3 mm height). Details about the synchrotron X-ray and imaging process are given in [19].

3. Results and discussion

3.1. Surface roughness and pore analyses

Figure 2 shows optical micrographs from the vertical sections and the corresponding surface topology of the samples captured using SEM. At low laser scan speed, keyhole porosity associated with high laser power dominated the parts. High energy input resulted in higher penetration of laser in the base plate and an increased depth-to-width ratio of the "J" shaped vapor cavity inside the melt pool. Higher depth-to-width ratios of the keyhole vapor cavity increase the chance of keyhole tip pinching off and trapping pores inside the part after solidification leading to spherical keyhole pores [33,34]. Increasing the laser scan speed (up to 1250 mm/s) decreases the laser penetration, thus, lowering the likelihood of keyhole porosity.

As the scan speed increases, the melt pool decreases in cross-section resulting in insufficient penetration in relation to the hatch spacing thus, lack of fusion (LoF) defects with non-spherical morphology are formed. LoF defects form for various reasons in addition to insufficient overlap between the adjacent melt tracks, such as irregular powder packing and melt pool instability [35–38]. In the current study, the relatively large particle size (i.e., larger than laser beam diameter) of the non-spherical powder resulted in a higher chance of the "shadowing effect" [39]. This phenomenon occurs when a powder particle or large spatters ejected from the powder bed block the laser beam and cause melt pool instability and consequent defects in the part [18].

SEM micrographs showing the top surface topology of the parts are shown in Figure 2. Surface defects were generated due to melt pool fluctuations under high laser energy input, and they typically appeared at low scan speeds. High power at low scan speed (e.g., P = 370 W and V = 400 mm/s) resulted in high turbulence in the met pool and protrusions outside the melt pool, thus, created surface defects on the top surface of the L-PBF parts [40]. In other words, increasing laser scan speed tends to reduce the melt pool instability and result in smoother top surfaces as demonstrated in Figure 2. The sample produced with P = 370 W and V = 1500 mm/s showed relatively smooth surface topology, however, this power-velocity combination resulted in the formation LoF porosity in the final parts. It was concluded that the presence of the keyhole porosity was directly correlated with the presence of the top surface defects (e.g., rough surface finish and open pores); however, LoF porosity formed at higher scan speeds of 1500 mm/s where no balling defect appeared on the top surface.

Figure 2b shows optical micrographs from the vertical sections manufactured using varying P in the range of 225-370 W and V = 1250 mm/s. The LoF porosity defects dominated the parts when low laser power of 225 W was used and by increasing the laser power, the amount of LoF defects was reduced and a trace amount of keyhole pores started to emerge. Even though the LoF

pores were visible on the cross-section of the sample fabricated by P = 225 W, the top surface did not show any balling defects

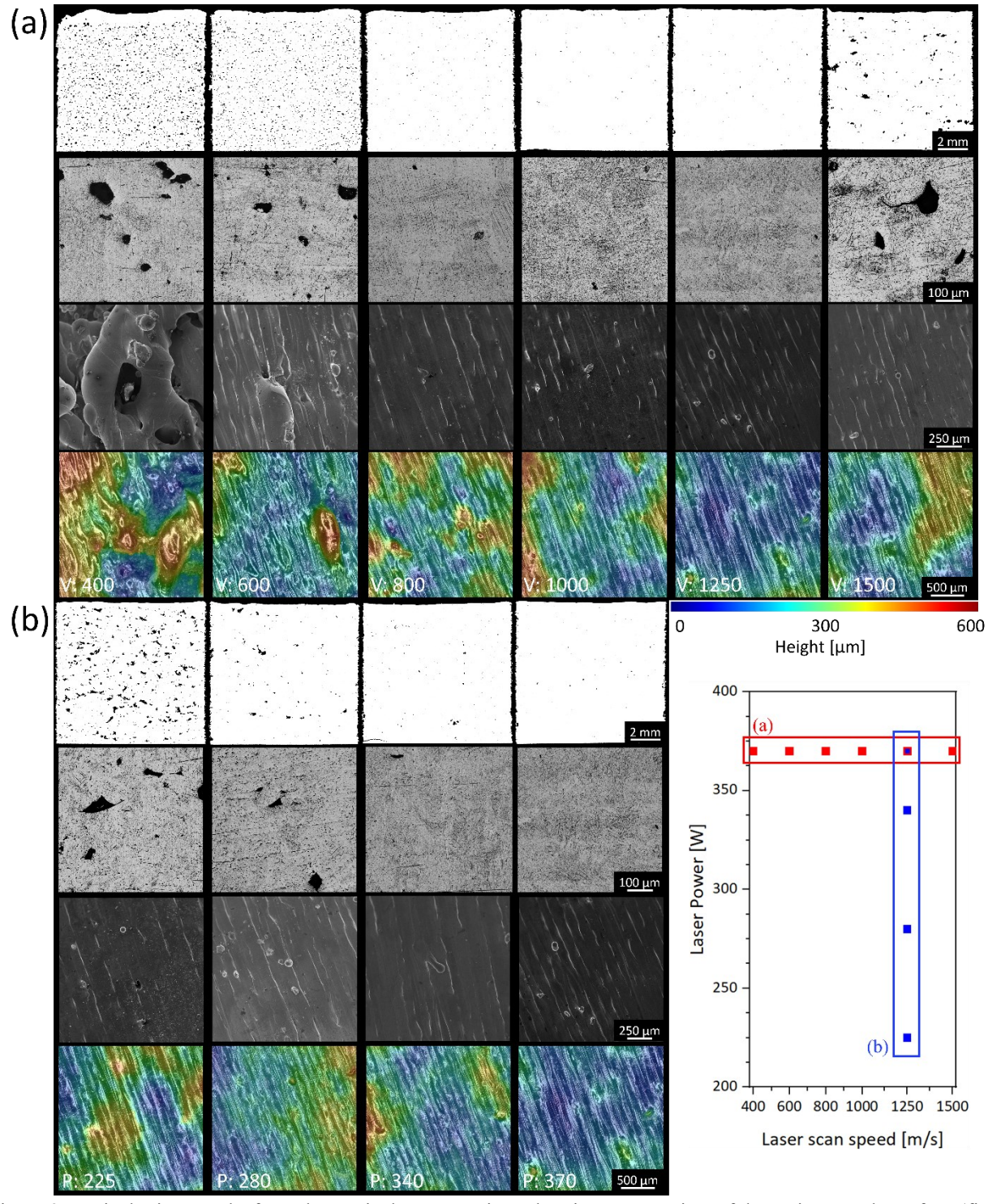


Figure 2. Optical micrographs from the vertical cross-sections showing an overview of the entire sample surface (first row) and etched surface at higher magnification (second row). SEM images (third row) and optical surface topography profiles (fourth row) collected from the top surface of the L-PBF processed HDH Ti-6Al-4V parts manufactured using (a) P = 370 W and varying laser scan speed of 400-1500 mm/s and (b) V = 1250 mm/s and varying laser power of 225-370 W. The diagram on the right shows the overview of the laser parameters used in this study.

Attempts have been made to predict the occurrence of LoF porosities in the L-PBF processed parts using various parameters. One of the widely used parameters in the AM community is the volumetric energy density (VED), however, it has been reported that VED is not a robust parameter to be used for predicting the porosity formation [19,35]. Therefore, other critical parameters, e.g., melt pool width (W), melt pool depth (D), hatch spacing (H), and layer thickness (L), were used to introduce a geometric model by Tang et al. [35] for predicting the occurrence of LoF porosities inside the P-V space. This geometric model (Eq. 1) captures the main reason for presence of LoF porosities (i.e., insufficient melting) as a function of different parameters as follows:

$$\left(\frac{H}{W}\right)^2 + \left(\frac{L}{D}\right)^2 \le 1 \tag{Eq. 1}$$

The melt pool shape is assumed to be semi-circular such that W = 2D and the hatch spacing is the center-to-center distance between the adjacent melt pools. In addition, the melt pool depth D can be estimated using differentiation and approximation of the Rosenthal equation [41,42]:

$$D = \sqrt{\frac{2Q\varepsilon}{\pi e \rho C_p V(T_m - T_0)}}$$
 (Eq. 2)

where Q is power (W), ε is absorptivity (0.48), e is the base of natural logarithms, ρ is density (4430 kg/m³), C_p is specific heat capacity (526 J/kg.K), V is the scan speed (mm/s), T_m is the melting temperature (K), and T_0 is the pre-heat temperature (K) [1,43].

The defined geometric model was applied to the dataset in the current study and the results are shown in Figure 3. Increasing the laser power increases the melt pool depth and width, thus, reduces the $\frac{H}{W}$ and $\frac{L}{D}$ ratios and bringing the samples under the boundary, i.e., removing the keyhole porosities which was shown in Figure 2b as well. On the other hand, increasing the laser scan speed decreases the depth and width of the melt pool, thus, moves the samples toward the LoF boundary. The shift from keyhole porosities in the low scan speed range (i.e., $V \le 800$ mm/s) to LoF porosities in the high scan speed range (i.e., $V \ge 1500$ mm/s) can be seen in both Figure 3 and Figure 2a. Generally, wider and deeper melt pools are required for adequate overlap between adjacent melt pools, however, one should avoid excessive depth of the melt pool because of material evaporation at the tip of the keyhole and the consequent keyhole porosity. Thus, keyhole depth should be controlled by altering the processing parameters such as laser scan speed, as will be discussed in subsection 3.2.

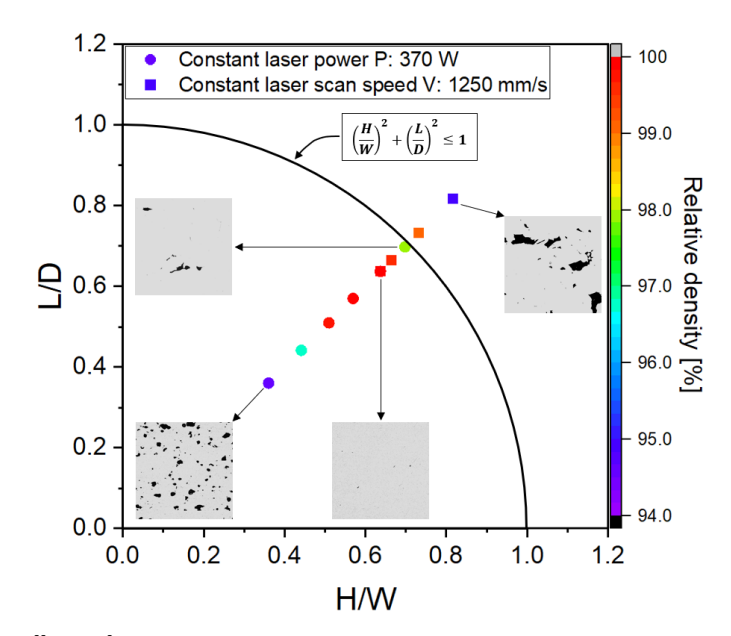


Figure 3. Processing map of $\frac{H}{W}$ and $\frac{L}{D}$ ratios of the L-PBF processed non-spherical Ti-6Al-4V powder. Inset images show the optical micrographs taken from the vertical cross-section of the parts showing the porosity content and type. $\frac{H}{W}$ and $\frac{L}{D}$ combination that fall withing the circular arc prevent the occurrence of LoF porosity.

Quantitative surface roughness analysis as a function of the L-PBF processing parameters are shown in Figure 4. At P=370 W, increasing the laser scan speed from 400 to 800 mm/s decreased the top surface average surface roughness from $S_a=119$ µm to $S_a=18.68$ µm. The significant reduction in the top surface roughness was a direct result of reduction in melt pool and keyhole instability [40]. Further increase in V up to 1500 mm/s maintained the average surface roughness in the range of $S_a=16.28$ µm to $S_a=21.5$ µm. These quantitative analyses suggested when P/V ratio was between 0.2 and 0.5, surface roughness was independent of P and V. Also, at V=1250 mm/s, the average surface roughness fluctuated between $S_a=16.23$ µm and $S_a=21.43$ µm with increasing P from 225 to 370 W (Note that these fluctuations are not statistically significant due to the measurement errors). Therefore, slow scan speeds (i.e., \leq 600 mm/s at P=370 W) had a significant impact on the surface roughness of the L-PBF processed non-spherical Ti-6Al-4V powder, while for higher laser scan speed (i.e., 600 mm/s < velocity < 1500 mm/s) there was minimal variation in the top surface roughness. Figure 4b shows average surface roughness against P/V ratio. It is obvious that increasing P/V ratio results in higher surface roughness, but this behavior was only significant for P/V > 0.5.

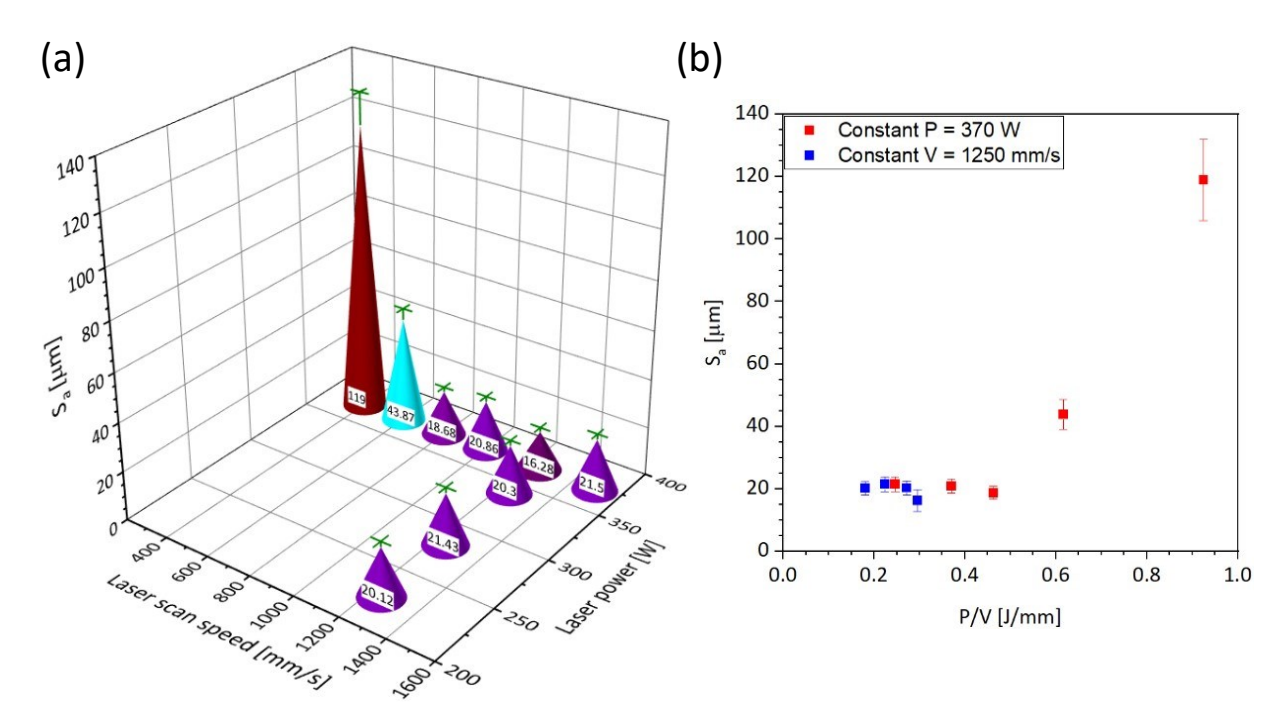


Figure 4. (a) The measured average surface roughness taken from the top surface as a function of laser power and velocity, and (b) the average surface roughness values against P/V ratio. Note that the numbers on the cones in (a) are the average measured S_a values.

The impact of L-PBF processing parameters on the porosity content was studied in terms of the number of pores per 100 mm² against the pores' equivalent spherical diameter (ESD), Figure 5. With increasing V up to 1000 mm/s, the total number of pores decreased from 5773 to 437. Further increases in V up to 1500 mm/s resulted in more pores such that the total number of pores increased to 799 and 1203 at V = 1250 mm/s and V = 1500 mm/s, respectively. Despite the increase in pore count when the scan speed was increased from 1000 mm/s to 1250 mm/s, the relative density of the part increased by 0.03% (see Table 1). In other words, porosity size was smaller when a laser scan speed of 1250 mm/s was applied compared to 1000 mm/s. Regarding the effect of laser power on the porosity content, increasing the laser power at V = 1250 mm/s resulted in reduction of the total number of porosities, thus, increased the relative density of the L-PBF processed non-spherical Ti-6Al-4V parts. Comparing our results with samples printed with nominal parameters using fine spherical powder, it was demonstrated that much higher build rate could be achieved and still have a relative density of > 99.5 %. In other words, there is a process window available for this non-spherical HDH Ti-6Al-4V powder to achieve the desired relative density. Further microstructural observations are conducted to understand if microstructure control is possible within this process window and results are presented in the next section.

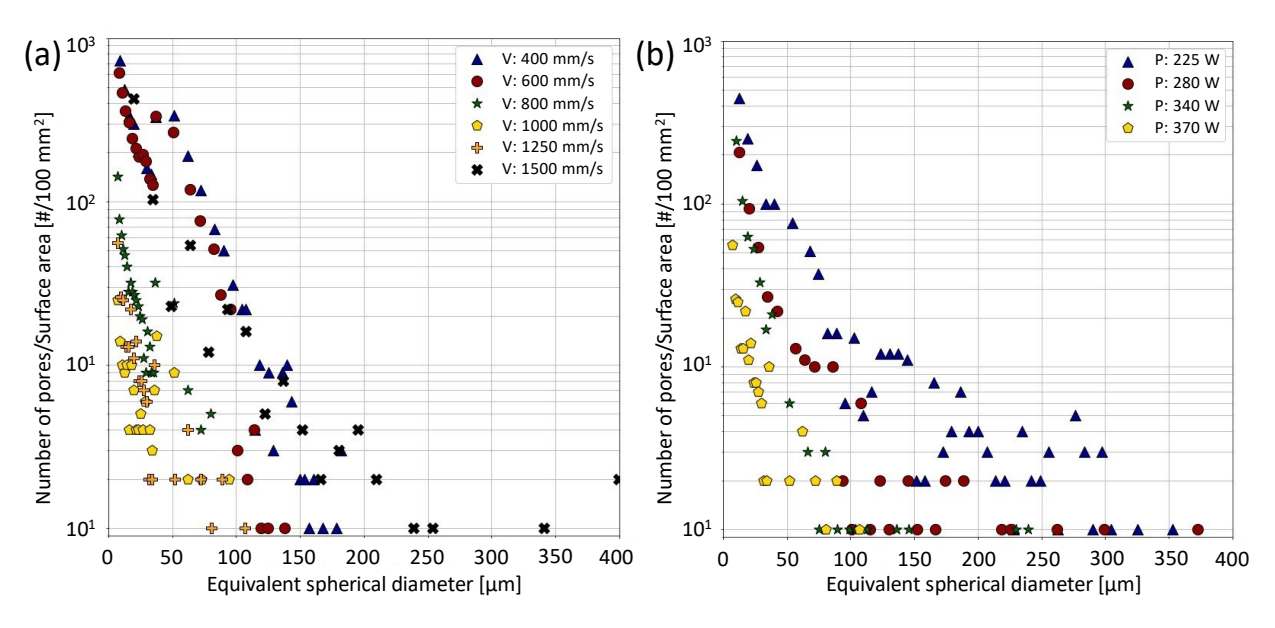


Figure 5. Number density of pores against ESD; (a) P = 370 W and varying laser scan speeds, and (b) V = 1250 mm/s and varying laser power. Note that the number of pores was normalized by the surface area of the vertical cross-section of each sample to obtain number density.

Table 1. Processing parameters used for L-PBF of HDH Ti-6Al-4V powder. Nominal L-PBF parameters were provided by EOS company for Ti-6Al-4V using spherical powder with median size of $d_{50} = 39 \mu m$. The layer thickness of 30 μ m and hatch spacing of 120 μ m were used by the EOS company. Build rate and energy density were calculated based on [19] and results were given in the table.

Sample No.	Laser powder [W]	Laser scan speed [mm/s]	Relative density [%]	Build Rate [mm ³ /s]	Energy Density [J/mm³]
1	370	400	94.59	2.88	128.47
2	370	600	96.69	4.32	85.64
3	370	800	99.67	5.76	64.23
4	370	1000	99.85	7.2	51.38
5	370	1250	99.88	9	41.11
6	370	1500	97.91	10.8	34.25
7	225	1250	94.92	9	25
8	280	1250	99.07	9	31.11
9	340	1250	99.66	9	37.77
Nominal	340	1250	99.55	4.5	75.5

3.2. Melt pool analysis using dynamic X-ray radiography

The DXR data was used to analyze the influence of laser scan speed on the keyhole instability and the results are shown in Figure 6. Here, P = 350 W and V changed between 400-1200 mm/s. Figure 6a demonstrates that as V increased from 400 mm/s to 1200 mm/s, the mode changed from unstable keyholing (i.e., \leq 500 mm/s) to stable keyhole mode (i.e., 700 mm/s) and conduction mode (i.e., 1200 mm/s). The analyzed keyhole depth is shown in Figure 6b. Analyzed data showed continuous reduction in the average and standard deviation of the measured keyhole depth by increasing the laser scan speed from 400 mm/s to 1200 mm/s. Higher scan speeds reduce the time for penetration into the powder and base plate, thus, decreasing the keyhole depth. The reduction of standard deviation of the measured keyhole depth suggested that the axial keyhole instability decreased with the increase in laser scan speed. The keyhole width measurement results are shown in Figure 6c. As the scan speed increases, the keyhole width gradually increases. Overall, with

increasing V, keyhole depth decreases but the lateral heat increases, thus, slightly increasing the melt pool width.

One of the explanations for the keyhole depth fluctuations is the "shadowing effect" as hypothesized by Zhao et al. [33]. Powder particles or spatters temporarily block the laser path and result in lower penetration of the laser light. Additionally, Khairallah et al. [39] demonstrated that a laser parameter threshold can intensify the "shadowing effect" and the keyhole depth fluctuations. In the current study, the standard deviation in keyhole depth values decreased abruptly from 26.8 μ m to 13.4 μ m as V increased from 400 to 500 mm/s. Thus, a scan speed of 500 mm/s is approximately the threshold between the high and low keyhole depth fluctuations regions and amplification of the "shadowing effect".

Low laser scan speed not only results in a deeper keyhole, but also results in a higher rate of laser reflections from the front keyhole wall that cause instability of the rear keyhole wall. Keyhole width measurements were carried out to capture this radial instability of the keyhole, and the standard deviation of the keyhole width showed that the radial instability decreased with increasing scan speed. During laser melting, most of the incident laser beam contacts the front keyhole wall [44,45]. Also, the front keyhole wall angle increases as V decreases (see Figure 6e) and becomes larger than the critical Brewster's angle thus significantly decreasing the laser absorption [33]. Low laser absorption on the front keyhole wall at high angles leads to more reflections from the front keyhole wall to the rear keyhole wall, thus, instability at low V.

3.3. Microstructure and texture evolution

To investigate the effect of laser power and scan speed on microstructure and grain evolution of L-PBF processed HDH Ti-6Al-4V powder, EBSD IPF-Z maps from the vertical cross-section as well as the reconstructed prior β grains and related pole figures were gathered and are shown in Figure 7. Prior β grains were reconstructed using (i) the Burgers Orientation Relationship (BOR) between the hexagonal closed pack (HCP) and body centered cubic (BCC) crystal structures governing the $\beta \rightarrow \alpha$ transformation [46] for instance $[0001]_{\alpha} \parallel [110]_{\beta}$ and $[2\ \bar{1}\ \bar{1}\ 0]_{\alpha} \parallel [\bar{1}\ 1\ \bar{1}]_{\beta}$, (ii) a minimum misorientation of 2.5°, and (iii) the triple junction method to select the common prior β grain for different martensite grains [47]. At P = 370, the melt pool depth decreased with an increased laser scan speed from 400 mm/s to 1500 mm/s based on Eq. 2.

As the melt pool depth decreases because of higher V, the laser penetration into the previously deposited layers also decreases, thus, the remelting rate declines. A higher fraction of remelting during laser melting results in much closer general orientation between the neighboring prior β grains as shown in Figure 7. Closer orientation results in higher degree of anisotropy inside the AM part and this phenomenon can be seen in the pole figures provided in Figure 7. It is worth noting that the points regarding the relationship between the general orientation of the prior β grains and the remelting rate is true when an asymmetric scan rotation (e.g., 67°) between the layers is applied. When symmetric scan rotations such as 0° or 90° are used, the randomness in the texture of the prior β grains is reduced significantly and typically long columns of prior β grains form inside the fusion-based processed AM part [48–50].

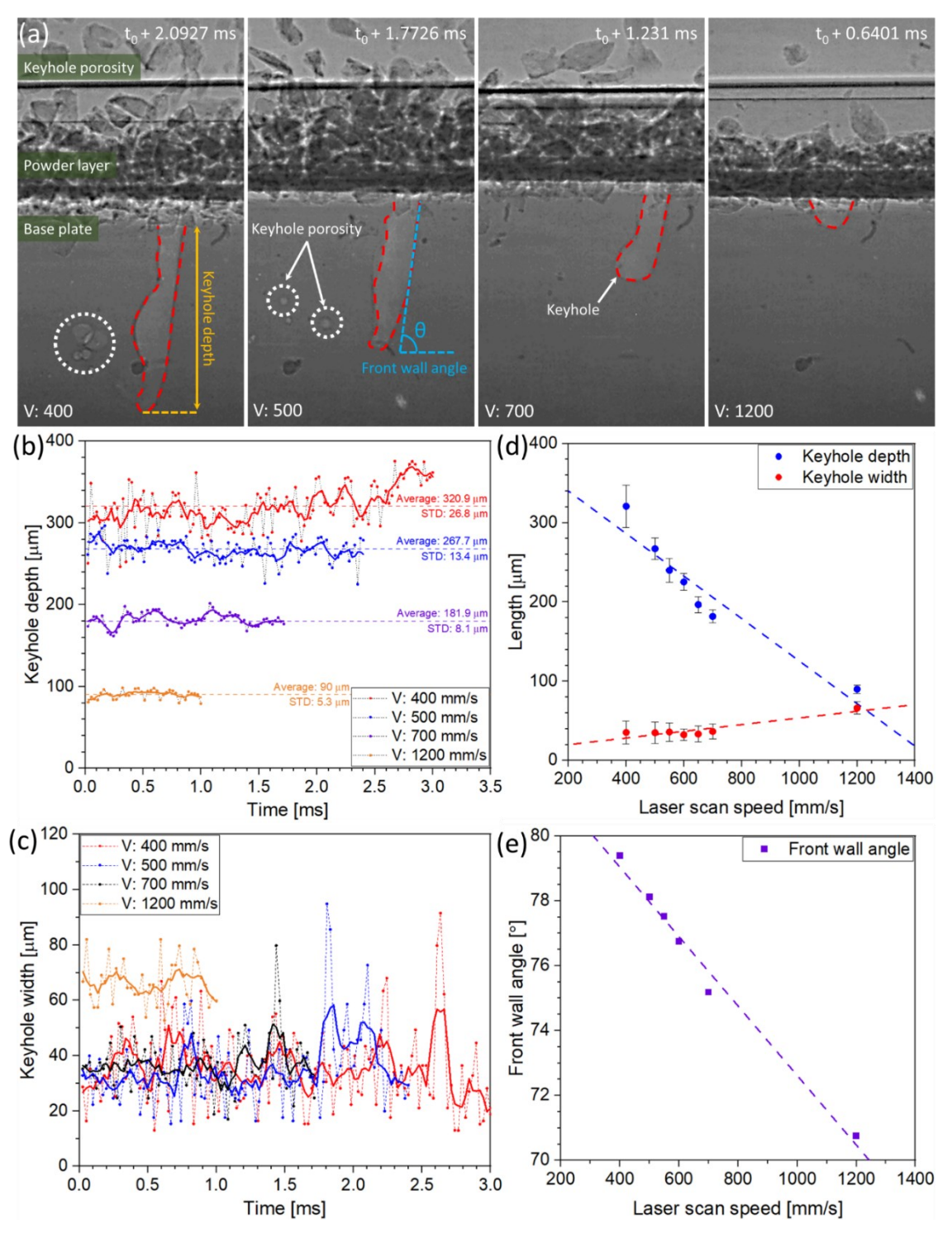


Figure 6. (a) DXR frames collected in the powder added single-bead Ti-6Al-4V experiments at P = 350 W and varying laser scan speeds of 400, 500, 700, and 1200 mm/s showing the keyholes, keyhole porosity, keyhole depth, and keyhole front wall angle: (b) and (c) plot keyhole depth and width in each frame using the DXR data for the selected scan speeds, respectively; (d) average keyhole depth and width versus scan speed; (e) average keyhole front wall angle against scan speed. Note that the solid lines in (b) and (c) show the 5-point moving average, dashed lines in (b) show the average keyhole depth, dashed lines in (d) show the fitted line on the average keyhole depth and width data, and the dashed line in (e) shows a linear fit to the average keyhole front wall angle.

The same argument could be made when V = 1250 mm/s with an altering P between 225-370 W was applied. Higher P resulted in higher penetration depth of laser beam inside the AM part, thus, a deeper melt pool was achieved according to Eq. 2. With increasing P from 225 W to 370 W, the melt pool depth increased and the randomness in the L-PBF part decreased as indicated in pole figure results in Figure 7. This observation supported our hypothesis that a deeper melt pool resulted in less random orientation of prior β grains and higher anisotropy inside the AM part along the build direction. Note that the randomness of the texture in the parts produced using laser scan rotation of 67° is sensitive to the location of the EBSD scan. Although the EBSD data were collected from the middle of the sample, much larger scan areas and/or X-ray pole figures are needed to be able to draw an absolute conclusion regarding the randomness of the texture. In the current study, due to the number of the samples being studied, such data could not be collected. More detailed texture analysis with higher confidence will be presented in the future studies.

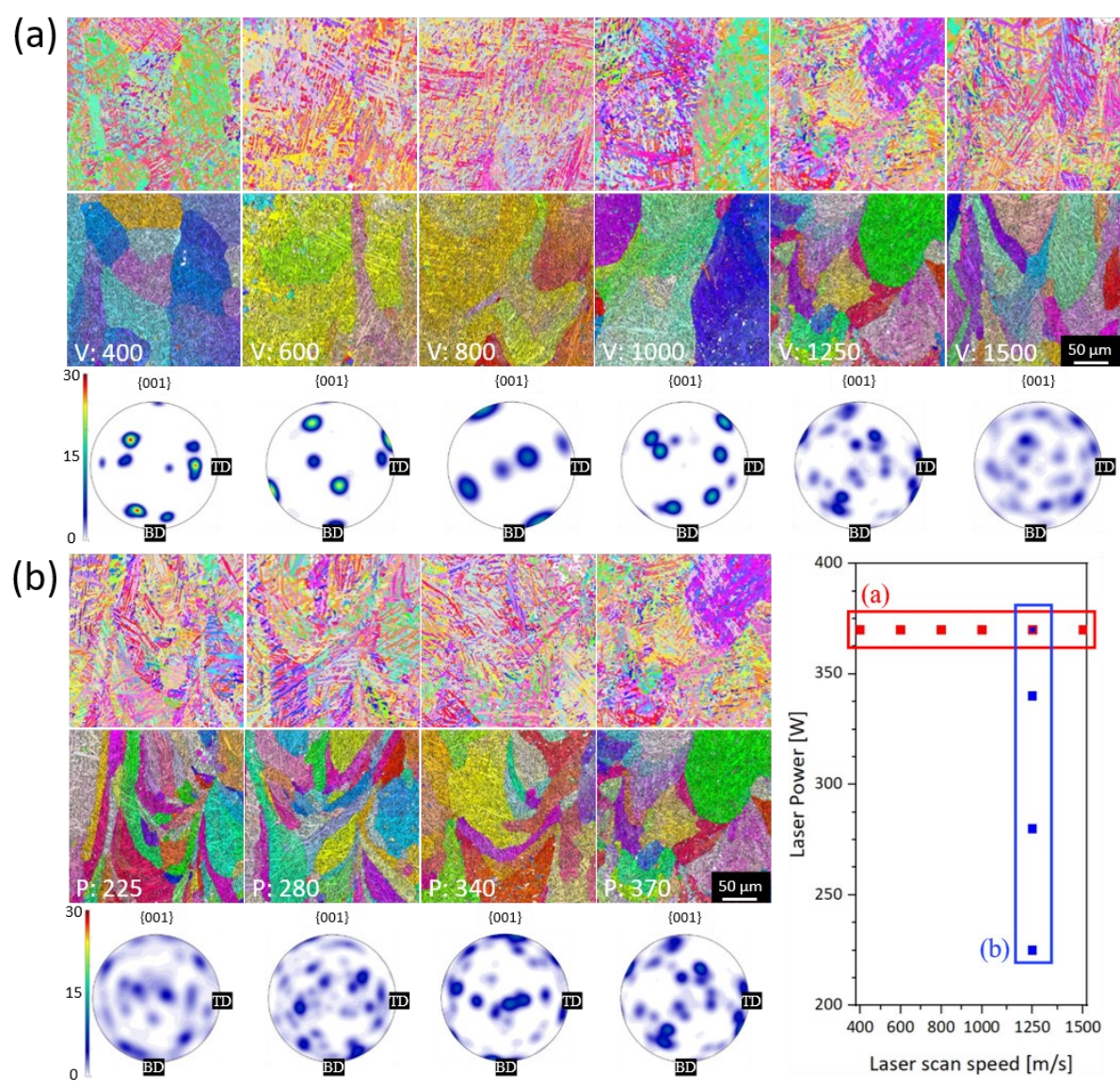


Figure 7. L-PBF processed non-spherical Ti-6Al-4V powder using (a) P = 370 at varying V ranging between 400-1500 mm/s and (b) V = 1250 mm/s at varying P ranging 225-370 W. In each group: (top) EBSD IPF-Z maps collected from the vertical cross-section, (middle) the corresponding reconstructed prior β grains on IPF-Z maps, and (bottom)

the corresponding pole figures extracted from the reconstructed prior β grains on IPF-Z maps. Note that the unit for the color bars of the pole figures is multiples of random distribution (MRD).

To quantitatively study the effect of processing parameters on anisotropy of the L-PBF parts, the maximum pole density from each prior β grains was plotted against the corresponding melt pool depth using Eq. 2 and results are shown in Figure 8. It was found that the relationship between the melt pool depth and anisotropy was linear when an asymmetric scan rotation was used. However, a symmetric scan rotation such as 90° would result in about similar heat transfer in melt pool, thus, similar prior β grain regrow with less than 2.5° misorientation regardless of the melt pool depth. Therefore, a highly elongated columnar prior β grains grow throughout the part and leading to a high anisotropy in the L-PBF part. When an asymmetric scan rotation such as 67° is applied, a similar laser path occurs after 360 layers. This would effectively interrupt the epitaxial growth of the prior β grains. Along with asymmetric scan rotations, instability of the melt pool and non-uniform thermal gradients [51] could lead to new prior β orientations known as stray grains [52]. Another reason for prior β grain boundary distortion is high laser scan speed which results in high temperature gradients between the edge and inner part of melt pool. Hence, distortion of epitaxial growth of the prior β grains is possible [53]. These observations showed that the anisotropy can be controlled in L-PBF processed HDH Ti-6Al-4V by using the appropriate scan rotation. Note that texture index [54] against the melt pool depth was plotted and the results are shown in Figure 8b. This complimentary plot provides a better overview of the texture strength in the parts by minimizing the sensitivity of data to the measurement techniques.

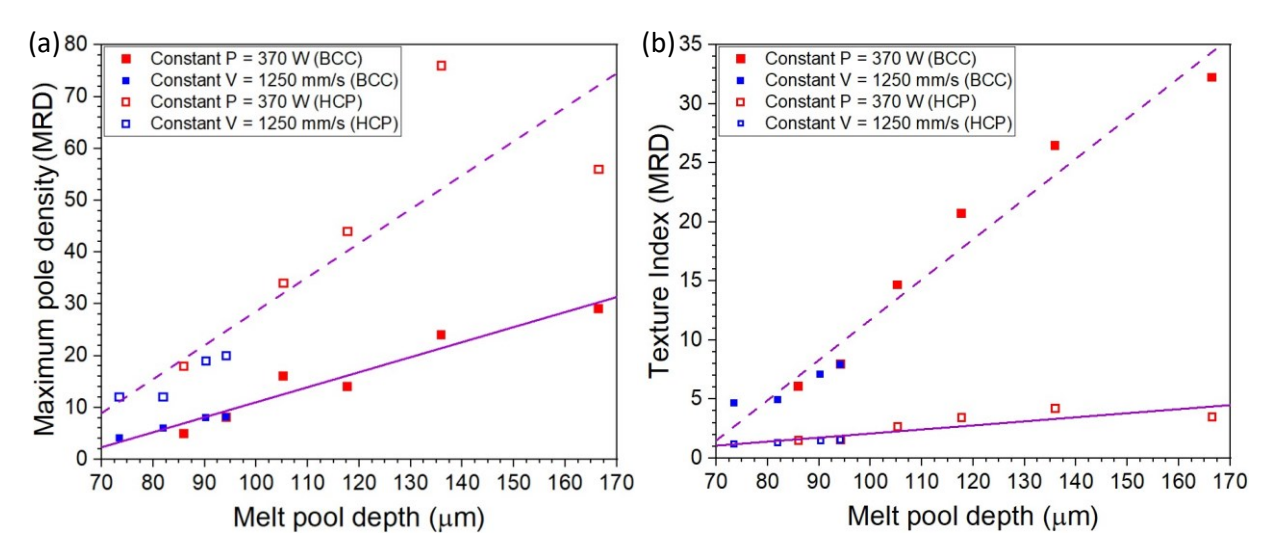


Figure 8. Calculated melt pool depth using Eq. 1 against the corresponding maximum pole density extracted from the pole figures in Figure 7. Note that the solid and dashed lines are the fitted lines on the BCC and HCP phases, respectively.

The effect of processing parameters on the prior β grain size and its morphology was studied by calculating the shape factor of each grain using the following equation:

$$SF = \frac{P}{EP}$$
 (Eq. 3)

where P is the measured perimeter of the grain, and EP is the calculated circle equivalent perimeter of the grain. When SF is closer to 1, it means that the grain is perfect circle and inversely, the higher the SF value, the more deviation from the perfect circle shape in the grain. The calculated SF values were plotted against the corresponding circle equivalent diameter of the grains and

results are shown in Figure 9. Note that the average number of analyzed prior β grains were ~15 grains in each scanned area, and prior β grains with the sizes smaller than the EBSD scan step size (i.e., 500 nm) were discarded. When low laser scan speed was applied, the prior β grains had an SF value closer to 1 (i.e., equiaxed grains) and by increasing the laser scan speed, the grains deviated more from the SF = 1 and exhibited SF values up to 5. Moreover, increasing the laser scan speed evidently limited the prior β grain size from the range of 20 to 240 μ m (V = 800 mm/s) to the range of 20 to 100 μ m (V = 1500 mm/s). This suggested when the laser scan speed was relatively low, the grains were larger and closer to equiaxed, whereas the grains were smaller and more elongated with increasing V. The effect of scan speed on the grain morphology is shown in Figure 7. A similar transition from equiaxed to columnar grains was also reported in laser direct energy deposited of Ti-6Al-4V alloy [55].

Regarding the effect of laser power on the prior β grain morphology, there was no direct effect on the shape of grains when the laser power increased, however, the size of the grains was slightly increased when P increased from 225 W to 370 W. The grains were more clustered with size ranging between 10 and 50 μ m at the applied laser power of 225 W, while they were more scattered with size ranging between 15 and 80 μ m at P = 340 W. Results indicated that V at a constant P was more influential in altering morphology and size the prior β grain. In other words, a variety of microstructure with grain morphology and size can be engineered using different L-PBF process parameters, while the final part density was kept above 99.5%.

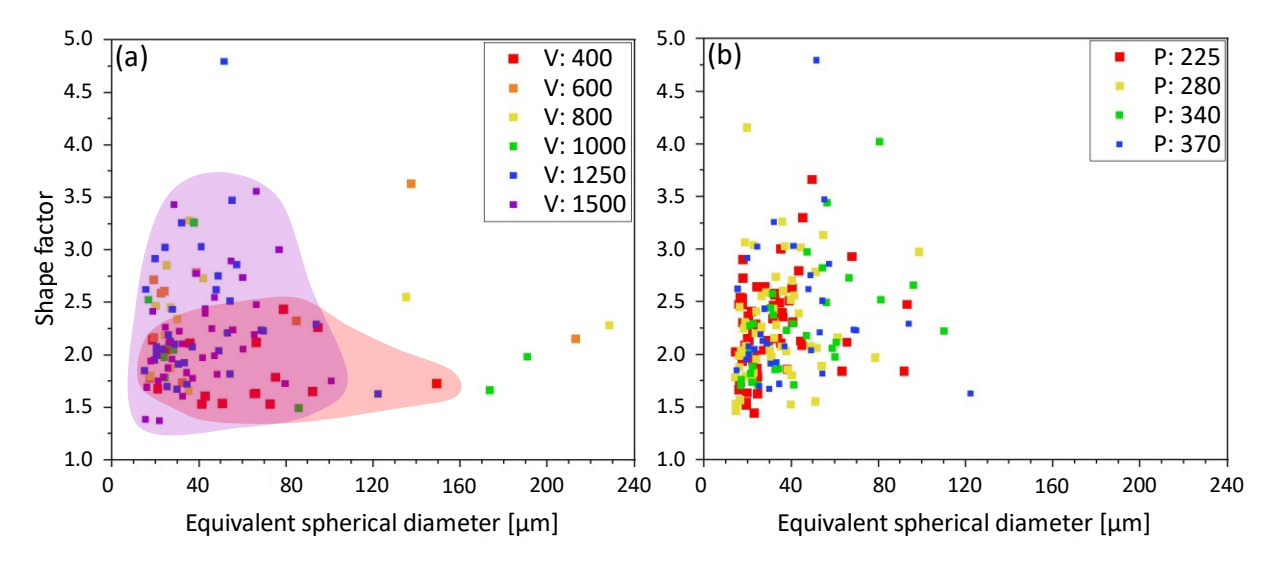


Figure 9. Shape factor of the prior β grains versus circle equivalent diameter: (a) P = 370 W and varying scan speed, and (b) V = 1250 mm/s and varying laser power. Red and blue regions in (a) show the calculated SF values against equivalent diameter for scan speeds of 400 mm/s and 1250 mm/s, respectively.

As mentioned before, $\beta \rightarrow \alpha$ transformation was strictly governed by the Burgers Orientation Relationship (BOR) between the crystal structure of β phase (BCC) and the crystal structure of α phase (HCP), defined as $\{0001\}_{\alpha} \parallel \{110\}_{\beta}$ and $\{1120\}_{\alpha} \parallel \{111\}_{\beta}$ and the transformation was schematically illustrated in Figure 10 [46]. Based on the BOR, 12 different α variations (see [31]) can form after $\beta \rightarrow \alpha$ transformation and 6 different β variations can form after $\alpha \rightarrow \beta$ transformation. The distribution of these 12 variants is not random and is controlled by the variant selection process [56,57]. Wang et al. [58] reported that the grain boundary between two adjacent α grains was formed based on 6 different types of misorientation called α/α boundary types. These types are defined as different misorientation axes and angles of 60° // [1 1 $\overline{2}$ 0] (type 2), 60.83° // [1.377 $\overline{1}$

2.377 0.359] (type 3), 63.26° // $[\overline{10}\ 5\ 5\ \overline{3}]$ (type 4), 90° // $[1\ \overline{2.38}\ 1.38\ 0]$ (type 5), 10.53° // [0001] (type 6), and low angle grain boundary between two α variants (type 1).

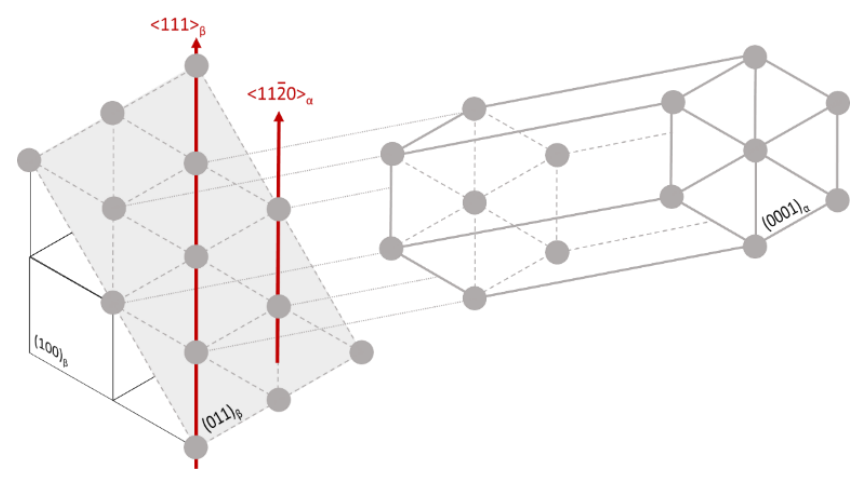


Figure 10. Schematic representation of the Burgers orientation relationship between the α (HCP) and β (BCC) phases in titanium alloys.

The misorientation distribution in the EBSD data can be used to measure the frequency of each type of α/α boundary. Figure 11a shows the misorientation distribution of α/α boundaries when P=370 W with varying V between 400-1500 mm/s. The results showed an obvious shift from the \sim 60° dominance to the \sim 63° dominance which qualitatively indicated the change in the dominance of different α/α boundary types. The calculated α/α boundary type (see Figure 11b) showed a gradual increase in the α/α boundary type 4 by increasing V from 400 mm/s to 1500 mm/s. This behavior was related to the increased cooling rate because of the increased laser scan speed. The cooling rates during the L-PBF process can be estimated using the Rosenthal equation [41,59,60]:

$$\frac{\partial T}{\partial t} = \left[1 + \frac{\xi}{\sqrt{\xi^2 + z^2}} + \frac{2\alpha\xi}{V(\xi^2 + z^2)}\right] \left(\frac{\lambda P}{2\pi k} \frac{V^2}{2\alpha} \frac{1}{\sqrt{\xi^2 + z^2}}\right) EXP\left[-\frac{V}{2\alpha} \left(\xi + \sqrt{\xi^2 + z^2}\right)\right]$$
(Eq. 4)

where ξ is relative distance to the center of the laser spot in x direction defined by (x - Vt) (mm), z is vertical distance from the center of the laser spot (mm), α is thermal diffusivity (2.87 × 10⁻⁶ m^2/s), V is laser scan speed (mm/s), P is laser power (W), k is thermal conductivity (6.7 W/m.K). Eq. 4 was used to estimate the cooling rate at two regions just under the remelted region and at the bottom of the previously deposited melt pool (see Figure 12a) under various processing parameters and the results are shown in Figure 12b. Results showed that cooling rate increases under the remelting region and decreases at the bottom of the previous melt pool by increasing V, and additionally, the difference between the cooling rates in both regions increases as V value increases because higher laser scan speed decreases the time for the temperature to be uniform between the regions. On the other hand, the change in laser power had no significant effect on the α/α boundary type distribution as the change in laser scan speed. This happens because the sensitivity of cooling rates to P is much less than V. Two reasons can be mentioned for the effect of laser power to be less than laser scan speed on the cooling rate: (i) in the Eq. 4, the laser speed has an exponential effect on the cooling rate, while, the effect of laser power is roughly linear (see Figure 12), and (ii) the range of changing laser scan speed (400 to 1500 mm/s) is much larger than the laser power (225 to 370 W), thus, the effect of laser scan speed is more amplified in the calculations.

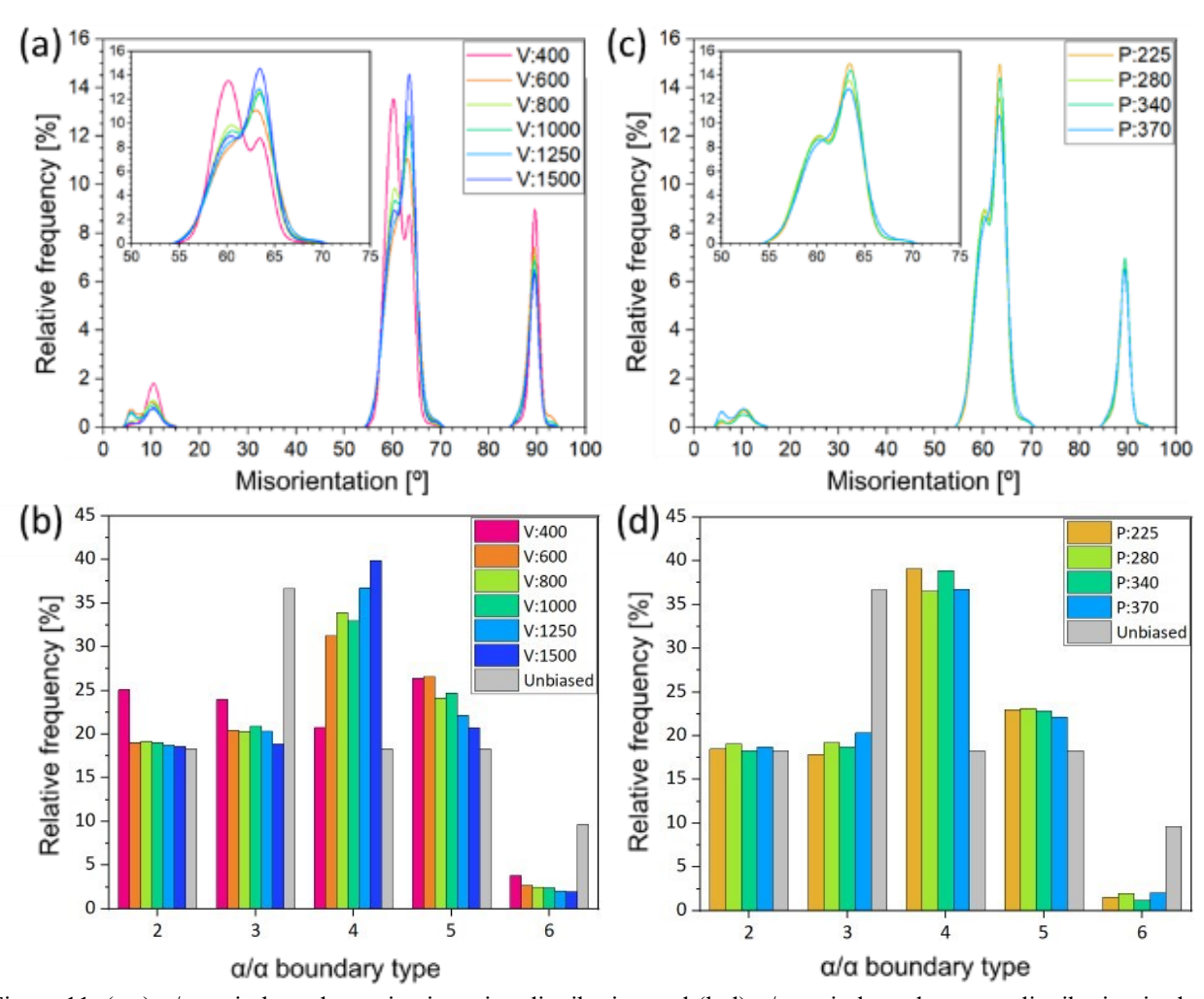


Figure 11. (a,c) α/α grain boundary misorientation distribution and (b,d) α/α grain boundary type distribution in the case of (a,b) constant laser power of 370 W and varying laser scan speed of 400-1500 mm/s and (c,d) constant laser scan speed of 1250 mm/s and varying laser power of 225-370 W.

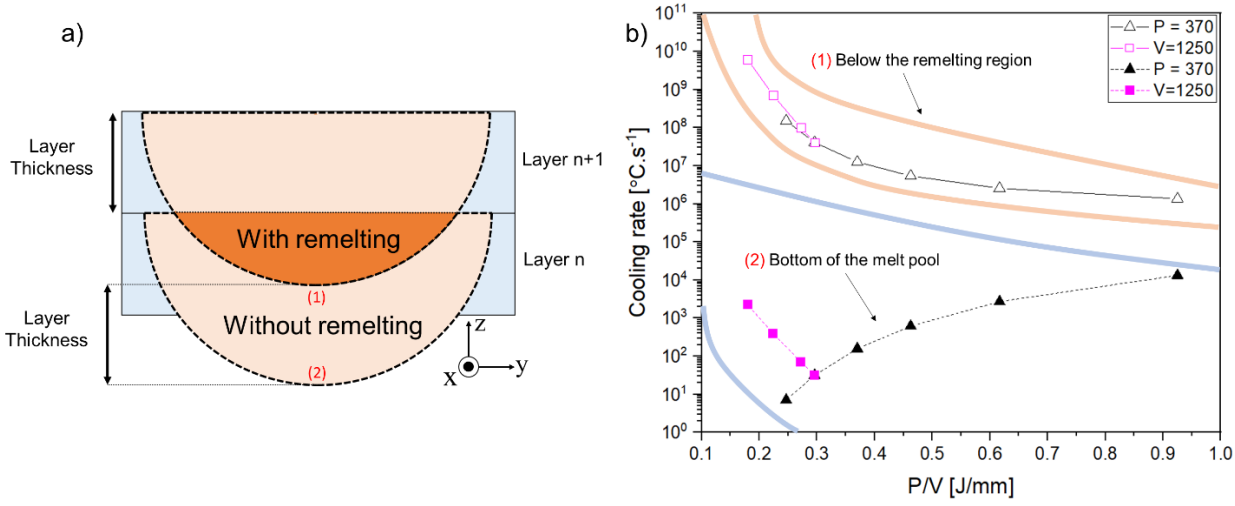


Figure 12. (a) Schematic representation of two melt pools in two consecutive layers showing with and without remelting regions, and (b) estimated cooling rates based on the Rosenthal equation against the P/V ratio. Note that the

blue and orange lines in (b) show the estimated cooling rate regions for the "bottom of the melt pool" and "below the remelting region", respectively.

The significant change in the dominance of α/α boundary type by increasing the laser scan speed indicates the change in the self-accommodating cluster dominance as well. Self-accommodation is the process of shape strain minimization through nucleation of triple α variants. The possible triple α variants with the highest rate of shape strain minimization were calculated by Wang *et al.* [58] and classified in two main categories; Category I which is the group of A-B-C, D-E-F, G-H-I, and J-K-L variants and Category II which is the group of A-E-I, B-D-L, C-G-K, and F-H-J variants. Category I and Category II are associated with the type 2 and type 4 α/α grain boundary variants, respectively. Therefore, by increasing the laser scan speed, the dominance of the Category I cluster type gradually changes to Category II. In addition to the measurement of α/α boundary types, the degree of variant selection (DVS) can be calculated using the following equation [61]:

$$DVS = \sum_{i}^{6} |P_{t,i} - P_{e,i}|$$
 (Eq. 5)

where P_t is relative frequency of occurrence of each α/α boundary type when no variant selection is present, P_e is relative frequency of experimentally measured α/α boundary types, and i is α/α boundary type counter which can take integers from one to six. The DVS can be any number between zero (in the case of no variant selection) and 1.833 (in the case of selection of just one α/α boundary type).

For each sample, the power-to-scan speed ratio (P/V) was calculated, and the DVS was plotted against this ratio (see Figure 13). The results showed an inverse relationship between the DVS and the P/V ratio. The general relationship showed that the DVS was controllable by altering the laser parameters. In our previous effort [19], we showed that increasing the P/V results in reduction of cooling rate. Here the data suggested that increasing the P/V results in reduction of DVS, meaning that the amount of variant selection decreased. Thus, it can be concluded lower cooling rates result in weaker variant selection. The cooling rate had a direct effect on the internal stresses introduced in the part during the printing process as reported by Ref. [62,63]. They reported that increasing P or decreasing V (i.e., increasing the cross-sectional area of the melt pool) results in lower cooling rates, more uniform shape changes inside and outside of the melt pool, and consequently, lower residual stress in the parts. The internal residual stress and applied shear stress affected the variant selection process as reported by Zhang et al. [64]. Moreover, Shi et al. [65] investigated the influence of local stress on the variant selection process using phase-field simulation and reported that a shear stress along a specific direction intensifies the variant selection.

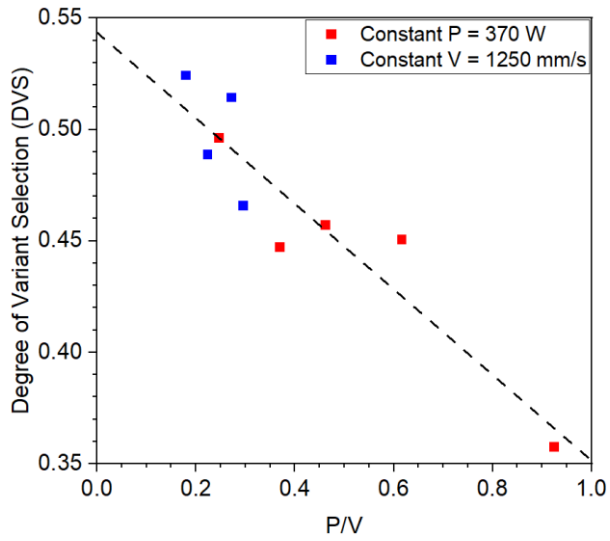


Figure 13. Degree of variant selection against the P/V ratio.

3.4. Microhardness

Microhardness tests were carried out on non-spherical Ti-6Al-4V powder that was produced using L-PBF, and the results are illustrated in Figure 14. By increasing the laser scan speed from 400 mm/s to 1000 mm/s, a \sim 30 HV_{0.5} enhancement in hardness was observed, from 359.3 HV_{0.5} to 389.3 HV_{0.5}. This enhancement in hardness is directly linked to the elimination of almost all of the porosities in the parts, as shown in Figure 2 and Table 1. Interestingly, increasing the laser scan speed further to 1250 mm/s resulted in a decrease of \sim 6.5 units in hardness. This variation could be due to measurement errors. Nonetheless, the change in hardness between samples with relative densities of > 99.8% could be a result of variations in thermal history and microstructural details (i.e., lamellar vs martensitic microstructure). The lower microhardness values of the sample fabricated using a laser scan speed of 1500 mm/s were connected to the higher fraction of pores introduced to the L-PBF-processed HDH Ti-6Al-4V part, since the applied process parameters fell into the LoF index and formation of shallow melt pool.

At a laser scanning speed of 1250 mm/s, raising the laser power from 225 W to 370 W resulted in an increase in microhardness from 355.5 HV0.5 to 382.9 HV0.5. Similar to the previous

discussion about how porosity affects microhardness, the L-PBF process part with a higher relative density at a laser power of 370 W had a higher microhardness.

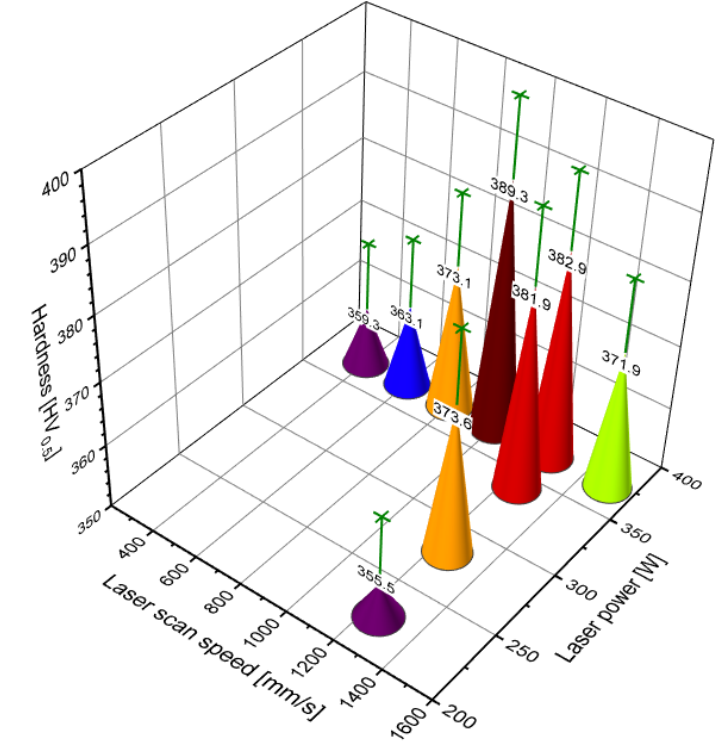


Figure 14. Vickers microhardness as a function of laser power and laser scan speed collected from the parts fabricated using L-PBF process of non-spherical Ti-6Al-4V powder.

4. Conclusion

In this research, the impact of laser power and scanning speed on the development of microstructure, defects, and microhardness of the HDH Ti-6Al-4V components produced through L-PBF was explored. The following findings can be inferred:

- In the area where the scanning speed was low, the most common type of pore was keyhole porosity. As the scanning speed was raised while keeping the laser power constant, these keyhole porosities disappeared, and further increases in scanning speed led to the formation of LoF pores. Conversely, in the area where the laser power was low, LoF pores were present and could be eliminated by raising the laser power. At low laser scan speed, surface roughness showed severe intrusion and extrusions due to the high melt pool turbulences during the L-PBF process. Increasing the laser scan speed resolved the issue and resulted in a smoother top surface even when the LoF pores were present in the final parts at a maximum scan speed of 1500 mm/s. Interestingly, in the low laser power region where the LoF pores were present, the top surface of the part was relatively smooth with an average roughness between 16 μm to 27 μm. In other words, we found that presence of keyhole porosity within the bulk part may be correlated with high surface roughness, but presence of LoF is not correlated with surface roughness.
- Microscopy observations including EBSD analysis suggested that the prior β grain morphologies gradually changed from larger equiaxed grains to smaller columnar

grains, the intense anisotropic texture was relieved to be more random. Also, the dominant α/α boundary type changed from type 2 to type 4, and the degree of variant selection was significantly decreased by increasing the laser scan speed. In contrast, increasing the laser power did not have any noticeable impact on the microstructure and the overall morphology of the prior β grains did not change, whereas the texture became slightly less random. We also observed that the dominant α/α boundary type remained as type 4 and the degree of variant selection decreased slightly.

• The behavior of the molten pool was examined through DXR examination, and it was discovered that melt pools with greater depth generated more directional texture in both previous β crystals and α' laths. A reverse correlation was identified between the P/V ratio and the level of variant selection in the non-spherical Ti-6Al-4V components fabricated using L-PBF.

Acknowledgements

AM acknowledges startup funding from Mechanical, Materials and Aerospace Engineering Department at Illinois Institute of Technology at Chicago, Illinois. Authors acknowledge partial support from the National Science Foundation under grant number DMR-2050916. Also, this work is supported in part by the Pennsylvania Infrastructure Technology Alliance, a partnership of Carnegie Mellon, Lehigh University and the Commonwealth of Pennsylvania's Department of Community and Economic Development (DCED). The authors recognize Reading Alloys (formerly affiliated with AMETEK Inc., now a part of Kymera International), especially Mike Marucci, for providing the Ti-6Al-4V powder used in this work, and assistance with the study. This work was performed under the auspices of the U.S. Department of Energy by Lawrence Livermore National Laboratory under contract DE-AC52-07NA27344 and IM release number # LLNL-JRNL-844166. This research used resources of the Advanced Photon Source, a U.S. Department of Energy (DOE) Office of Science user facility operated for the DOE Office of Science by Argonne National Laboratory under Contract No. DE-AC02-06CH11357.

References

- [1] M.J. Donachie, Titanium: a technical guide, (2000).
- [2] C. Cui, B. Hu, L. Zhao, S. Liu, Titanium alloy production technology, market prospects and industry development, Mater. Des. 32 (2011) 1684–1691.
- [3] Y.-L. Hao, S.-J. Li, R. Yang, Biomedical titanium alloys and their additive manufacturing, Rare Met. 35 (2016) 661–671.
- [4] C. Emmelmann, P. Sander, J. Kranz, E. Wycisk, Laser additive manufacturing and bionics: redefining lightweight design, Phys. Procedia. 12 (2011) 364–368.
- [5] L. Parry, I.A. Ashcroft, R.D. Wildman, Understanding the effect of laser scan strategy on residual stress in selective laser melting through thermo-mechanical simulation, Addit. Manuf. 12 (2016) 1–15.
- [6] R.K. Gupta, V.A. Kumar, C. Mathew, G.S. Rao, Strain hardening of titanium alloy Ti6Al4V sheets with prior heat treatment and cold working, Mater. Sci. Eng. A. 662 (2016) 537–550.
- [7] C. de Formanoir, A. Brulard, S. Vivès, G. Martin, F. Prima, S. Michotte, E. Rivière, A. Dolimont, S. Godet, A strategy to improve the work-hardening behavior of Ti–6Al–4V parts produced by additive manufacturing, Mater. Res. Lett. 5 (2017) 201–208.

- [8] A.V.S.R. Prasad, K. Ramji, G.L. Datta, An experimental study of wire EDM on Ti-6Al-4V alloy, Procedia Mater. Sci. 5 (2014) 2567–2576.
- [9] A. Uriondo, M. Esperon-Miguez, S. Perinpanayagam, The present and future of additive manufacturing in the aerospace sector: A review of important aspects, Proc. Inst. Mech. Eng. Part G J. Aerosp. Eng. 229 (2015) 2132–2147.
- [10] D.P. Barbis, R.M. Gasior, G.P. Walker, J.A. Capone, T.S. Schaeffer, Titanium powders from the hydride-dehydride process, in: Titan. Powder Metall. Sci. Technol. Appl., Elsevier Inc., 2015: pp. 101–116.
- [11] A. Loukanov, N. El Allaoui, A. Omor, F.Z. Elmadani, K. Bouayad, N. Seiichiro, Oxidation behavior of low-cost CP-Ti powders for additive manufacturing via fluidizatio, J. Neurol. Sci. (2020) 116544.
- [12] Q. Tao, Z. Wang, G. Chen, W. Cai, P. Cao, C. Zhang, W. Ding, X. Lu, T. Luo, X. Qu, M. Qin, Selective laser melting of CP-Ti to overcome the low cost and high performance tradeoff, Addit. Manuf. 34 (2020) 101198.
- [13] A. Mostafaei, C. Zhao, Y. He, S. Reza Ghiaasiaan, B. Shi, S. Shao, N. Shamsaei, Z. Wu, N. Kouraytem, T. Sun, J. Pauza, J. V. Gordon, B. Webler, N.D. Parab, M. Asherloo, Q. Guo, L. Chen, A.D. Rollett, Defects and anomalies in powder bed fusion metal additive manufacturing, Curr. Opin. Solid State Mater. Sci. 26 (2022) 100974.
- [14] F. Medina, Reducing metal alloy powder costs for use in powder bed fusion additive manufacturing: Improving the economics for production, The University of Texas at El Paso, 2013.
- [15] S.P. Narra, Z. Wu, J. Capone, M. Paliwal, A.D. Rollett, Use of Non-Spherical Hydride-DeHydride (HDH) Powders in Powder Bed Fusion Additive Manufacturing, Addit. Manuf. 34 (2020) 101188.
- [16] H. Jaber, T. Kovacs, K. János, Investigating the impact of a selective laser melting process on Ti6Al4V alloy hybrid powders with spherical and irregular shapes, Adv. Mater. Process. Technol. (2020) 1–17.
- [17] J. Varela, E. Arrieta, M. Paliwal, M. Marucci, J.H. Sandoval, J.A. Gonzalez, B. McWilliams, L.E. Murr, R.B. Wicker, F. Medina, Investigation of Microstructure and Mechanical Properties for Ti-6Al-4V Alloy Parts Produced Using Non-Spherical Precursor Powder by Laser Powder Bed Fusion, Materials (Basel). 14 (2021) 3028.
- [18] Z. Wu, M. Asherloo, R. Jiang, M.H. Delpazir, N. Sivakumar, M. Paliwal, J. Capone, B. Gould, A. Rollett, A. Mostafaei, Study of Printability and Porosity Formation in Laser Powder Bed Fusion Built Hydride-Dehydride (HDH) Ti-6Al-4V, Addit. Manuf. 47 (2021) 102323.
- [19] M. Asherloo, Z. Wu, E. Ghebreiesus, S. Fryzlewicz, R. Jiang, B. Gould, M. Heim, D. Nelson, M. Marucci, M. Paliwal, A.D. Rollett, A. Mostafaei, Laser-beam powder bed fusion of cost-effective non-spherical hydride-dehydride Ti-6Al-4V alloy, Addit. Manuf. 56 (2022) 102875.
- [20] T. Vilaro, C. Colin, J.D. Bartout, As-fabricated and heat-treated microstructures of the Ti-6Al-4V alloy processed by selective laser melting, Metall. Mater. Trans. A Phys. Metall. Mater. Sci. 42 (2011) 3190–3199.
- [21] J. Yang, H. Yu, J. Yin, M. Gao, Z. Wang, X. Zeng, Formation and control of martensite in Ti-6Al-4V alloy produced by selective laser melting, Mater. Des. 108 (2016) 308–318.
- [22] M. Asherloo, Z. Wu, M. Heim, D. Nelson, M. Paliwal, A.D. Rollett, A. Mostafaei, Fatigue performance of laser powder bed fusion hydride-dehydride Ti-6Al-4V powder, Addit.

- Manuf. 59 (2022) 103117.
- [23] X. Zhou, D. Xu, S. Geng, Y. Fan, C. Yang, Q. Wang, F. Wang, Microstructural evolution and corrosion behavior of Ti–6Al–4V alloy fabricated by laser metal deposition for dental applications, J. Mater. Res. Technol. 14 (2021) 1459–1472.
- [24] N. Kazantseva, P. Krakhmalev, M. Thuvander, I. Yadroitsev, N. Vinogradova, I. Ezhov, Martensitic transformations in Ti-6Al-4V (ELI) alloy manufactured by 3D Printing, Mater. Charact. 146 (2018) 101–112.
- [25] M. V Pantawane, S. Dasari, S.A. Mantri, R. Banerjee, N.B. Dahotre, Rapid thermokinetics driven nanoscale vanadium clustering within martensite laths in laser powder bed fused additively manufactured Ti6Al4V, Mater. Res. Lett. 8 (2020) 383–389.
- [26] A. Zafari, M.R. Barati, K. Xia, Controlling martensitic decomposition during selective laser melting to achieve best ductility in high strength Ti-6Al-4V, Mater. Sci. Eng. A. 744 (2019) 445–455.
- [27] W. Xu, M. Brandt, S. Sun, J. Elambasseril, Q. Liu, K. Latham, K. Xia, M. Qian, Additive Manufacturing of Strong and Ductile Ti-6Al-4V by Selective Laser Melting via In Situ Martensite Decompisition, Acta Mater. 85 (2015) 74–84.
- [28] A. Bustillo, E. Ukar, J.J. Rodriguez, A. Lamikiz, Modelling of process parameters in laser polishing of steel components using ensembles of regression trees, Int. J. Comput. Integr. Manuf. 24 (2011) 735–747.
- [29] M. Simonelli, Y.Y. Tse, C. Tuck, On the Texture Formation of Selective Laser Melted Ti-6Al-4V, Metall. Mater. Trans. A. 45 (2014) 2863–2872.
- [30] P.L. Stephenson, N. Haghdadi, R. DeMott, X.Z. Liao, S.P. Ringer, S. Primig, Effect of scanning strategy on variant selection in additively manufactured Ti-6Al-4V, Addit. Manuf. 36 (2020) 101581.
- [31] M. Asherloo, Z. Wu, J.E.C. Sabisch, I. Ghamarian, A.D. Rollett, A. Mostafaei, Variant selection in laser powder bed fusion of non-spherical Ti-6Al-4V powder, J. Mater. Sci. Technol. 147 (2023) 56–67.
- [32] C.A. Schneider, W.S. Rasband, K.W. Eliceiri, NIH Image to ImageJ: 25 years of image analysis, Nat. Methods. 9 (2012) 671–675.
- [33] C. Zhao, N.D. Parab, X. Li, K. Fezzaa, W. Tan, A.D. Rollett, T. Sun, Critical instability at moving keyhole tip generates porosity in laser melting, Science (80-.). 1086 (2020) 1080–1086.
- [34] R. Cunningham, C. Zhao, N. Parab, C. Kantzos, J. Pauza, K. Fezzaa, T. Sun, A.D. Rollett, Keyhole threshold and morphology in laser melting revealed by ultrahigh-speed x-ray imaging, Science (80-.). 363 (2019) 849–852.
- [35] M. Tang, P.C. Pistorius, J.L. Beuth, Prediction of Lack-of-Fusion Porosity for Powder Bed Fusion, Addit. Manuf. 14 (2017) 39–48.
- [36] H. Gong, K. Rafi, H. Gu, T. Starr, B. Stucker, Analysis of defect generation in Ti-6Al-4V parts made using powder bed fusion additive manufacturing processes, Addit. Manuf. 1 (2014) 87–98.
- [37] T. Mukherjee, T. DebRoy, Mitigation of lack of fusion defects in powder bed fusion additive manufacturing, J. Manuf. Process. 36 (2018) 442–449.
- [38] S. Coeck, M. Bisht, J. Plas, F. Verbist, Prediction of lack of fusion porosity in selective laser melting based on melt pool monitoring data, Addit. Manuf. 25 (2019) 347–356.
- [39] S.A. Khairallah, A.A. Martin, J.R.I. Lee, G. Guss, N.P. Calta, J.A. Hammons, M.H. Nielsen, K. Chaput, E. Schwalbach, M.N. Shah, M.G. Chapman, T.M. Willey, A.M. Rubenchik,

- A.T. Anderson, Y. Morris Wang, M.J. Matthews, W.E. King, Controlling interdependent meso-nanosecond dynamics and defect generation in metal 3D printing, Science (80-.). 368 (2020) 660–665.
- [40] H. Gong, H. Gu, K. Zeng, J.J.S. Dilip, D. Pal, B. Stucker, D. Christiansen, J. Beuth, J.J. Lewandowski, Melt pool characterization for selective laser melting of Ti-6Al-4V prealloyed powder, Solid Free. Fabr. Proc. (2014) 256–267.
- [41] D. Rosenthal, Mathematical theory of heat distribution during welding and cutting, Weld. J. 20 (1941) 220–234.
- [42] C.M. Adams Jr, Cooling rates and peak temperatures in fusion welding, Weld. J.(NY). 37 (1958).
- [43] G. Welsch, R. Boyer, E.W. Collings, Materials Properties Handbook: Titanium Alloys, ASM International, 1993.
- [44] A. Kaplan, A model of deep penetration laser welding based on calculation of the keyhole profile, J. Phys. D. Appl. Phys. 27 (1994) 1805–1814.
- [45] C. Zhao, Q. Guo, X. Li, N. Parab, K. Fezzaa, W. Tan, L. Chen, T. Sun, Bulk-Explosion-Induced Metal Spattering During Laser Processing, Phys. Rev. X. (2019).
- [46] W.G. Burgers, On the process of transition of the cubic-body-centered modification into the hexagonal-close-packed modification of zirconium, Physica. 1 (1934) 561–586.
- [47] F. Niessen, T. Nyyssönen, A.A. Gazder, R. Hielscher, Parent grain reconstruction from partially or fully transformed microstructures in {\it MTEX}, J. Appl. Crystallogr. 55 (2022) 180–194.
- [48] E. Fereiduni, A. Ghasemi, M. Elbestawi, Microstructural characterization and mechanical properties of nano-scale/sub-micron TiB-reinforced titanium matrix composites fabricated by laser powder bed fusion, J. Alloys Compd. 896 (2022) 163054.
- [49] L. Thijs, F. Verhaeghe, T. Craeghs, J. Van Humbeeck, J.P. Kruth, A study of the microstructural evolution during selective laser melting of Ti-6Al-4V, Acta Mater. 58 (2010) 3303–3312.
- [50] P.A. Kobryn, S.L. Semiatin, Microstructure and texture evolution during solidification processing of Ti-6A1-4V, J. Mater. Process. Technol. 135 (2003) 330–339.
- [51] J.G. Pauza, W.A. Tayon, A.D. Rollett, Computer simulation of microstructure development in powder-bed additive manufacturing with crystallographic texture, Model. Simul. Mater. Sci. Eng. 29 (2021) 55019.
- [52] J.M. Vitek, The effect of welding conditions on stray grain formation in single crystal welds theoretical analysis, Acta Mater. 53 (2005) 53–67.
- [53] Z. Wang, Z. Xiao, Y. Tse, C. Huang, W. Zhang, Optimization of processing parameters and establishment of a relationship between microstructure and mechanical properties of SLM titanium alloy, Opt. Laser Technol. 112 (2019) 159–167.
- [54] H.J. Bunge, Texture Analysis in Materials Science, edited by H.-J. Bunge, (1982).
- [55] X. Wu, J. Liang, J. Mei, C. Mitchell, P.S. Goodwin, W. Voice, Microstructures of laser-deposited Ti–6Al–4V, Mater. Des. 25 (2004) 137–144.
- [56] H. Inoue, S. Fukushima, N. Inakazu, Transformation Textures in Ti-15V-3Cr-3Sn-3Al Alloy Sheets, Mater. Trans. JIM. 33 (1992) 129–137.
- [57] J. Romero, M. Preuss, J. Quinta da Fonseca, Texture memory and variant selection during phase transformation of a zirconium alloy, Acta Mater. 57 (2009) 5501–5511.
- [58] S.C. Wang, M. Aindow, M.J. Starink, Effect of self-accommodation on α/α boundary populations in pure titanium, Acta Mater. 51 (2003) 2485–2503.

- [59] R. Fabbro, Melt pool and keyhole behaviour analysis for deep penetration laser welding, J. Phys. D. Appl. Phys. 43 (2010) 445501.
- [60] P. Promoppatum, S.C. Yao, P.C. Pistorius, A.D. Rollett, A Comprehensive Comparison of the Analytical and Numerical Prediction of the Thermal History and Solidification Microstructure of Inconel 718 Products Made by Laser Powder-Bed Fusion, Engineering. 3 (2017) 685–694.
- [61] D. Qiu, R. Shi, D. Zhang, W. Lu, Y. Wang, Variant selection by dislocations during α precipitation in α/β titanium alloys, Acta Mater. 88 (2015) 218–231.
- [62] C. Casavola, S.L. Campanelli, C. Pappalettere, Experimental analysis of residual stresses in the selective laser melting process, in: Proceedings XIth Int. Congr. Expo. Orlando, Florida, USA, 2008.
- [63] A.S. Wu, D.W. Brown, M. Kumar, G.F. Gallegos, W.E. King, An Experimental Investigation into Additive Manufacturing-Induced Residual Stresses in 316L Stainless Steel, Metall. Mater. Trans. A Phys. Metall. Mater. Sci. 45 (2014) 6260–6270.
- [64] J. Zhang, X. Li, D. Xu, R. Yang, Recent progress in the simulation of microstructure evolution in titanium alloys, Prog. Nat. Sci. Mater. Int. 29 (2019) 295–304.
- [65] R. Shi, Y. Wang, Variant selection during α precipitation in Ti–6Al–4V under the influence of local stress A simulation study, Acta Mater. 61 (2013) 6006–6024.